Project acronym and title:
SECURe – Subsurface Evaluation of Carbon capture and storage and Unconventional risks

A physics-informed constrained optimization workflow: maximizing injection while constraining induced seismicity at Oklahoma wastewater injection sites

Authors and affiliation:
Thibault Candela, Cintia Goncalves Machado, Olwijn Leeuwenburgh, Jan ter Heege

TNO Applied Geosciences

Email of lead author:
thibault.candela@tno.nl

D5.6
Revision:1 (draft for definitive)

Project funded by the European Commission within the Horizon 2020 Programme	
Dissemination Level	
PU	*Public*
~~***CO***~~	~~*Confidential, only for members of the consortium (incl. the Commission Services)*~~
~~***CL***~~	~~*Classified, as referred to in Commission decision 2001/844/EC*~~

Deliverable number:	**D5.6**
Deliverable name:	**A physics-informed constrained optimization workflow: maximizing injection while constraining induced seismicity at Oklahoma wastewater injection sites**
Work package:	**WP5 Impact Mitigation and Remediation**
Lead WP/deliverable beneficiary:	TNO

Status of deliverable		
	By	**Date**
Submitted (Author(s))	Thibault Candela	30/11/20
Verified (WP leader)	Pierre Cerasi	30/11/20
Approved (EB member)	Matteo Icardi	30/11/20
Approved (Coordinator)	E HOUGH	30/11/20

Author(s)		
Name	**Organisation**	**E-mail**
Thibault Candela	TNO	thibault.candela@tno.nl
Cintia Goncalves Machado	TNO	cintia.machado@tno.nl
Olwijn Leeuwenburgh	TNO	olwijn.leeuwenburgh@tno.nl
Jan ter Heege	TNO	jan.terheege@tno.nl

Public introduction

Subsurface Evaluation of CCS and Unconventional Risks (SECURe) is gathering unbiased, impartial scientific evidence for risk mitigation and monitoring for environmental protection to underpin subsurface geoenergy development. The main outputs of SECURe comprise recommendations for best practice for unconventional hydrocarbon production and geological CO2 storage. The project is funded from June 2018–May 2021.

The project is developing monitoring and mitigation strategies for the full geoenergy project lifecycle; by assessing plausible hazards and monitoring associated environmental risks. This is achieved through a program of experimental research and advanced technology development that includes demonstration at commercial and research facilities to formulate best practice. We will meet stakeholder needs; from the design of monitoring and mitigation strategies relevant to operators and regulators, to developing communication strategies to provide a greater level of understanding of the potential impacts.

The SECURe partnership comprises major research and commercial organisations from countries that host shale gas and CCS industries at different stages of operation (from permitted to closed). We are forming a durable international partnership with non-European groups; providing international access to study sites, creating links between projects and increasing our collective capability through exchange of scientific staff.

Executive report summary

A newly developed modelling framework is presented which specifically focusses on the Oklahoma case and the massive injection of wastewater, which led to a surge of induced seismicity. However, the modelling framework is versatile enough to be applied to any anthropogenic subsurface activities and should be seen as a good practice to maximize injection while minimizing induced seismicity. First, all the available a-priori knowledge is honored to deploy the simulation of the flow, induced stress changes and seismicity in the underground. Cutting-edge, full physics-based models are calibrated with observed seismicity data. Second, a constrained optimization approach is used for an efficient screening of multiple injection scenarios. Ultimately, an optimum theoretical scenario is identified which allows the maximization of injection volumes while keeping the seismicity level below a safe cap and, more specifically, would have prevented the rapid growth of the seismicity rate in 2015 in Oklahoma.

Contents

FIGURES

TABLES

1 Introduction

In response to the rapid increase of the rate of seismicity in 2015 in central and northern Oklahoma, the regulators decided in 2016 to reduce the total volume of injected brine (waste-product of production of shale gas) to less than 40% of the 2014 total volume (Ellsworth, 2013; Walsh and Zoback, 2015). Late 2016, large magnitude earthquakes were recorded, and in April 2017 all the wells were shut in. In 2016-2017, the detailed causal relation between injection operations and seismicity was unclear. In contrast, it is now well recognized and documented that the surge of the number of earthquakes in the central and northern Oklahoma can be attributed to the massive injection of brine in the subsurface (Keranen et al., 2014; Weingarten et al., 2015).

Multiple models have already been deployed to study either (i) the physical mechanisms at the origin of the induced events at Oklahoma (Johann et al., 2018; Goebel et al., 2017; Norbeck and Horne, 2016; Dempsey and Riffault, 2019) or (ii) to predict the return of the seismicity increase to a lower background rate after the stop of the injection activities in 2017 (Langenbruch and Zoback, 2016; Goebel et al., 2017; Langenbruch et al., 2018; Zhai et al., 2019). Up to now, these modelling strategies always involved simplifications either at the level of the simulations of the flow throughout the porous media (Goebel et al., 2017; Zhai et al., 2019) or at the level of the computations of the induced stress development and seismicity changes (Norbeck and Horne, 2016; Langenbruch and Zoback, 2016; Langenbruch et al., 2018; Johann et al., 2018; Dempsey and Riffault, 2019). In order to gain confidence in the predictive power of any modelling strategy, a thorough model validation against observed data is required. This step has largely been overlooked in existing modelling approaches of induced seismicity at Oklahoma which generally rely on simplified sensitivity analysis.

In this study, a novel modelling approach is outlined that is tailored to honor as much as possible available a priori knowledge at injection sites in the central Oklahoma area (for simplicity the area is simply referred to as Oklahoma in the remainder of the manuscript). A priori knowledge consists of data on local geology, flow, mechanical and seismicity response. The model parameters of our seismological model are conditioned with the observed seismicity in order to best fit the full spatio-temporal history of induced earthquakes. It is only after completing this data assimilation procedure that injection strategies can be optimized to maximize the volume of injected brine while minimizing induced seismicity. For optimizing injection strategies, we deployed a constrained optimization workflow that maximizes injection volumes under a fixed limit of allowed seismicity rate. Optimization results show with a different spatio-temporal injection history, the rapid growth of the seismicity rate in 2015 can be successfully prevented while the total volume of injected brine can even be increased. It indicates that injection operations and mitigation measures for induced seismicity greatly benefit from optimization of spatio-temporal injection strategies as seismic risks can be reduced under continuing injection operations.

2 Methodology

2.1 FLOW SIMULATIONS

The two main identified mechanisms that cause induced seismicity at Oklahoma are: (1) the slow diffusion of elevated pore pressure from the high-permeability Arbuckle aquifer (locus of the brine injections) to its low-permeability basement at the nucleation depth of the induced events (e.g. Norbeck and Horne, 2016; Langenbruch and Zoback, 2016; Dempsey and Riffault, 2019); (2) the change in total stress at this depth in the basement that is caused by poro-elastic loading due to the inflation of the rock volume associated with the increase in pore pressure (e.g. Goebel et al., 2017; Zhai et al., 2019).

The first modelling effort consists of assessing the historical spatio-temporal distribution of pore pressure changes caused by the massive injection of brine in the subsurface at Oklahoma. As in each step of our modelling strategy, this step aims to incorporate all the cumulated *a priori* knowledge on local geology, flow, mechanical and seismicity response at Oklahoma (Johnson, 2008; Faith et al., 2010; Keranen et al., 2013; Holland, 2013; Hinck et al., 2018; Pei et al., 2018). The computation of the pore pressure changes (*Figure 1*) is performed using the open source OPM-flow simulator (Open Porous Media Initiative, 2020, version 2020.04).

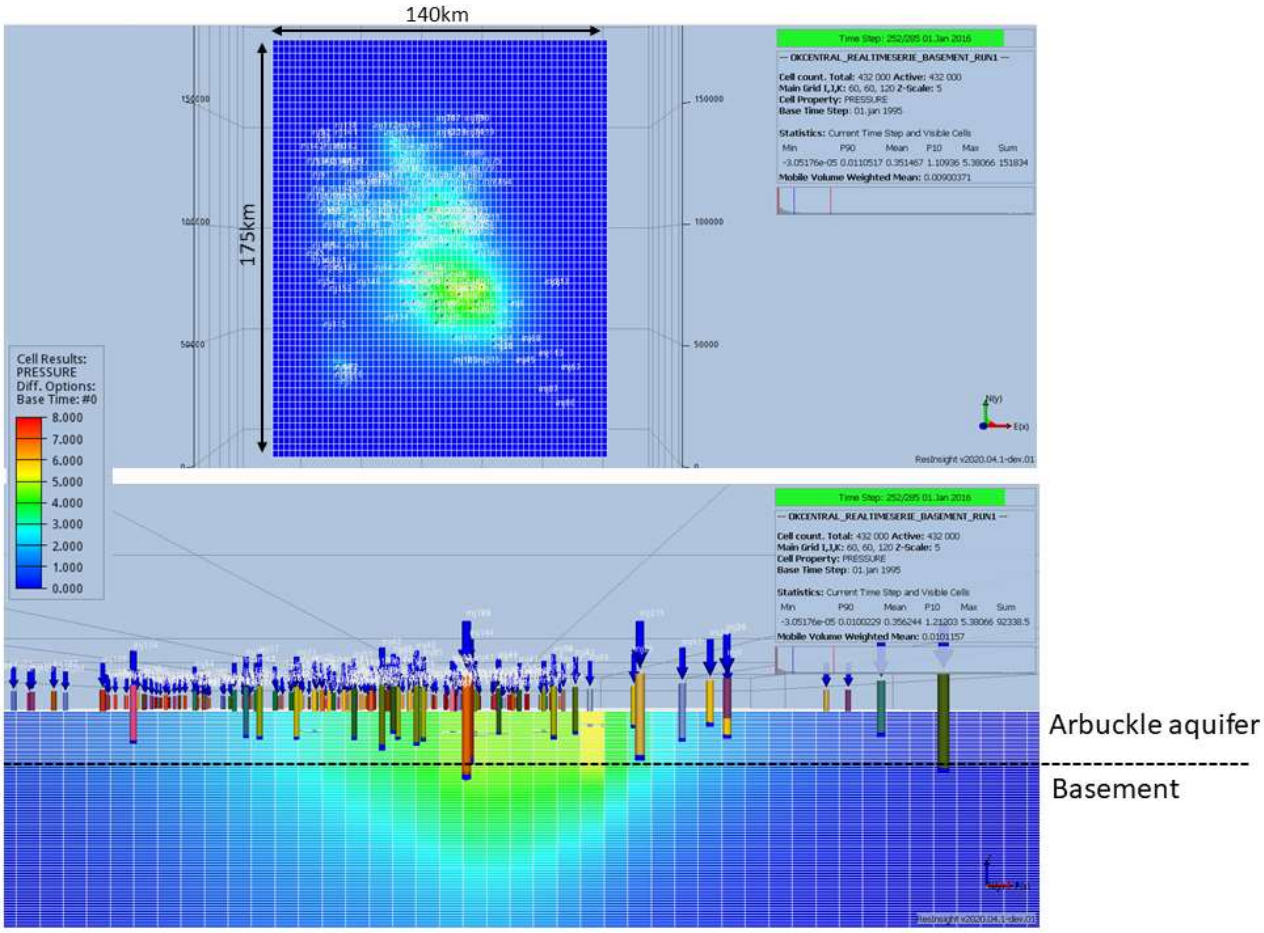

Figure 1: Flow simulation - visualization via ResInsight (open source visualization software, ResInsight [Computer Software], version 2020.10, part of Open Porous Media Initiative, Ceentron Solutions, 2020) *of the pressure field at the end of 2015.*

The flow model is populated by properties based on current understanding of the geological and hydrogeological settings at Oklahoma. Three layered-box models have been deployed, each of them including the same thickness for the Arbuckle aquifer and its basement but with different permeabilities and porosities (*Table 1*). Only the results of the flow simulation with a permeability of 50mD and 0.05mD for the Arbuckle aquifer and its basement, respectively, are discussed in this report (i.e. Model 1 in *Table 1*). This permeability contrast yields the most likely changes in pressures in the Arbuckle and its basement and is preferred to best match observations.

Table 1: Geometry and model parameters of the flow simulation models.

	Arbuckle			Basement		
	thickness	porosity	permeability	thickness	porosity	permeability
Model 1	1050m	0.22	50mD	5km	0.012	0.05mD
Model 2	1050m	0.12	5mD	5km	0.008	0.005mD
Model 3	1050m	0.22	50mD	5km	0.008	0.005mD

The OPM-FLOW simulation model honors the geographical location and depths of all the wells according to the Oklahoma Corporation Commission. It includes more than 200 wells for central Oklahoma, the focus area

for the present study, and for each of the well injectors the historical monthly injection rate from January 1995 to January 2018 is used as input (*Figure 2*). Note here that central and western Oklahoma can be considered as isolated and independent compartments in terms of flow (see Zhai et al. 2019); the same modelling complexities are attached to both areas of interest and solely focusing on central Oklahoma is considered sufficient to demonstrate the capabilities of the newly developed modelling framework. The injection depth at the Arbuckle level and distance to the basement has been reported as an important parameter correlated with the occurrence of the induced events (Hincks et al., 2018). The run-time of one full OPM-FLOW simulation from January 1995 to January 2018 takes less than 20 min, which is rather fast for such a complex flow simulation. The low computation time makes the simulations suitable for an ensemble-based approach that is used for the optimization. This optimization is the last step of our modelling approach (see Section 2.6).

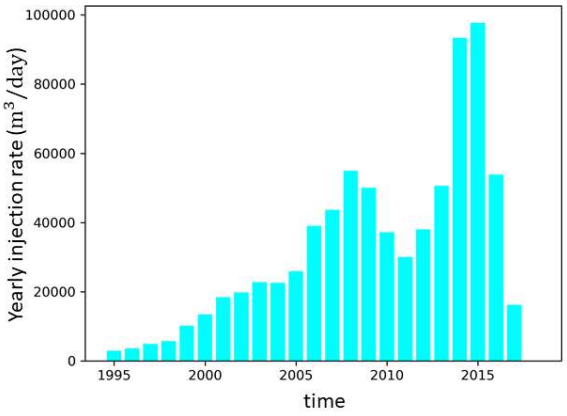

Figure 2: Historical yearly field-wide injection rate.

2.2 INDUCED STRESSES IN THE BASEMENT

The objective of this modelling step is to assess the spatio-temporal development of induced stresses at the earthquake nucleation depth, taken at approximately 4km depth based on the hypocenter locations of observed seismicity (McGarr and Barbour, 2017; Pei et al., 2018). The two main mechanisms that were identified to control induced stress development and earthquake nucleation at Oklahoma are included: (1) the decrease of the effective normal stress along the basement faults by pore pressure diffusion and (2) the changes in total stresses induced by poro-elastic effects associated with pressure increase and volumetric expansion of rock.

Our modelling approach assumes that highly permeable faults are hydraulically connecting the base of the Arbuckle aquifer to the basement. Simple calculations including typical fault properties (diffusivity, porosity, thickness) show that the diffusion time throughout the highly permeable faults-channels is on the order of at most a few days (Zhai et al. 2019). Therefore, one can assume that the changes in pore pressure modelled by OPM-FLOW at the base of the aquifer are representative of the changes in pore pressure at 4km depth experienced by the basement faults. These changes in pore pressures relatively to the start of injection and along a horizontal plane at 4km depth are shown in *Figure 3*. The increase in pore pressure is at first in 2009 localized at the center of the area of interest and then starts to progressively migrate towards the North-West.

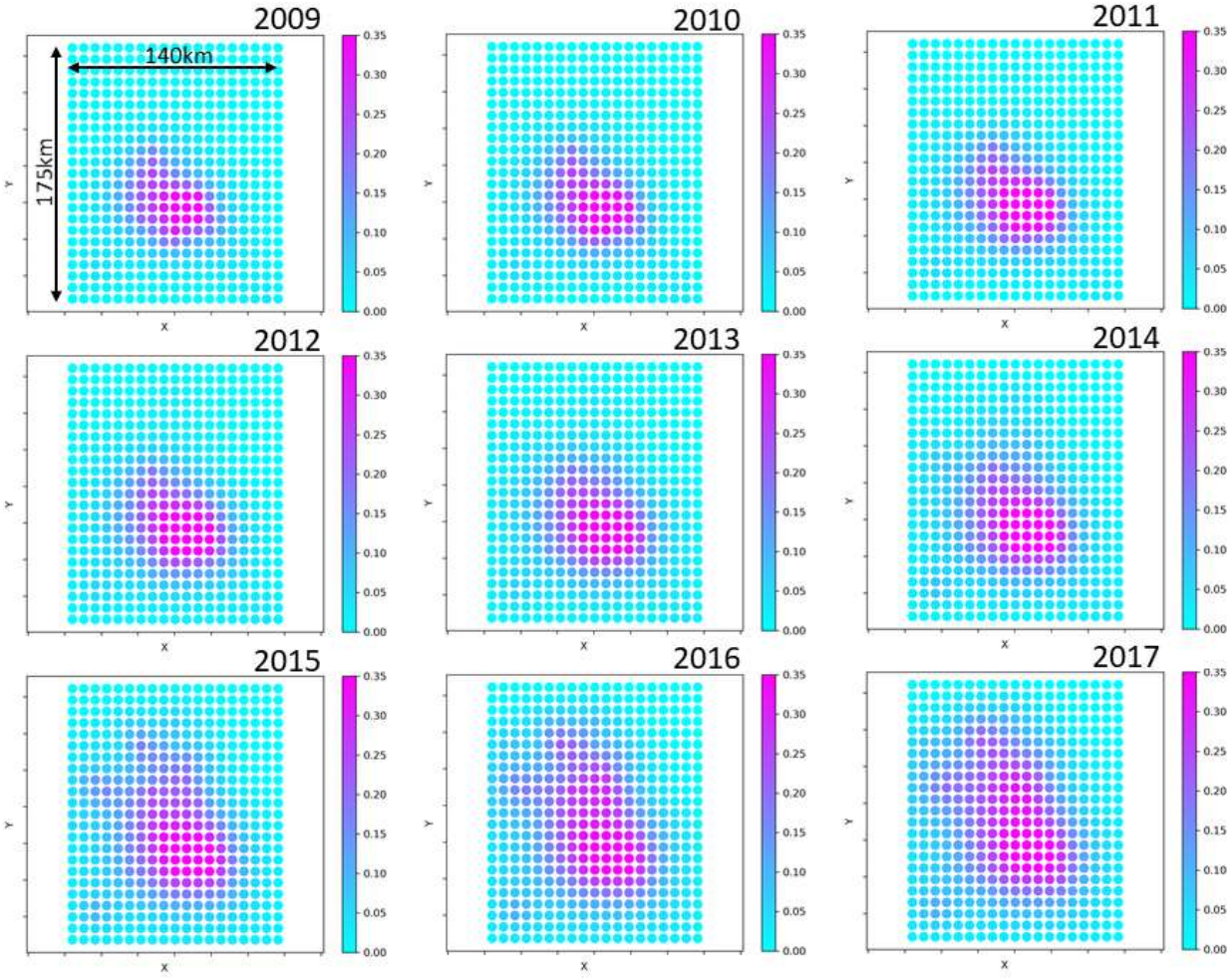

Figure 3: Changes in pore pressure (in MPa) at 4km depth along the basement faults.

From the spatio-temporal changes in pore pressures at 4km depth (*Figure 3*), the changes in the normal effective stress can be directly determined. Analogous to the analysis by Zhai et al. (2019), vertical strike-slip faults with a unique preferred fault strike azimuth of 50° are assumed to be ubiquitous in the basement. This faulting regime and the fault orientation is consistent with the statistical analysis of earthquake focal mechanisms and the in-situ stress analysis at Oklahoma (Alt and Zoback, 2016; Holland, 2013). Principal stresses are assumed to be spatially uniform around Oklahoma with a maximum horizontal stress azimuth oriented at 85°.

Changes in total stress imposed by the volumetric changes of the rock volume is determined using the in-house mechanical simulator MACRIS (Mechanical Analysis of Complex Reservoirs for Induced Seismicity, van Wees et al., 2019; Candela et al., 2019). The main advantage of MACRIS is that it is a mesh-free simulator, i.e. it does not need construction of a dedicated grid for the geomechanical analysis. MACRIS directly takes the grid of the flow simulation as input. In the present case, the grid consists of the 3D pressure fields computed by OPM-FLOW at a yearly sampling rate. Each grid block of the flow simulation is considered as an inflating/compacting nucleus of strain (or center of inflation/compaction, see Mindlin 1936; Geertsma, 1973; Okada, 1992). The contribution of each of these nuclei is integrated to compute the poro-elastic stress change at 4km depth in the basement. The Barnes-Hut algorithm (Barnes and Hut, 1986) is used for re-discretizing the initial flow grid. The purpose of using this algorithm is twofold: (i) to cluster the nuclei of strain close to the 4km depth horizontal plane in order to increase the spatial stress resolution, and (ii) to shorten the computation time. The approach has been validated by comparison with relatively slow finite-element numerical

computations in a previous study (van Wees et al., 2018). The poro-elastic normal and shear stress changes acting on the faults at 4km depth can thus be calculated using MACRIS. Coulomb stress changes can be evaluated by considering shear stresses and effective normal stresses:

$$S = \tau - [\mu - \alpha]\sigma_n' \quad (1)$$

where τ is the shear stress acting along the fault plane, σ_n' is the effective normal stress (which include the direct effect of the pore pressure increase intra-fault), μ is the coefficient of fault friction and α is a constitutive parameter (zero in this study). The Coulomb stress rate $\dot{S}$ along the horizontal plane at 4km depth is presented in *Figure 4*. As observed with the pore pressure fields, high Coulomb stress rates are first (in 2009) localized in the center of the area of interest, and then progressively migrates towards the North-West. In 2015, Coulomb stress rates are highly localized in the northwestern corner of the study area. Following the new measures imposed by the regulator, the Coulomb stressing rate starts to decrease and delocalize in 2016.

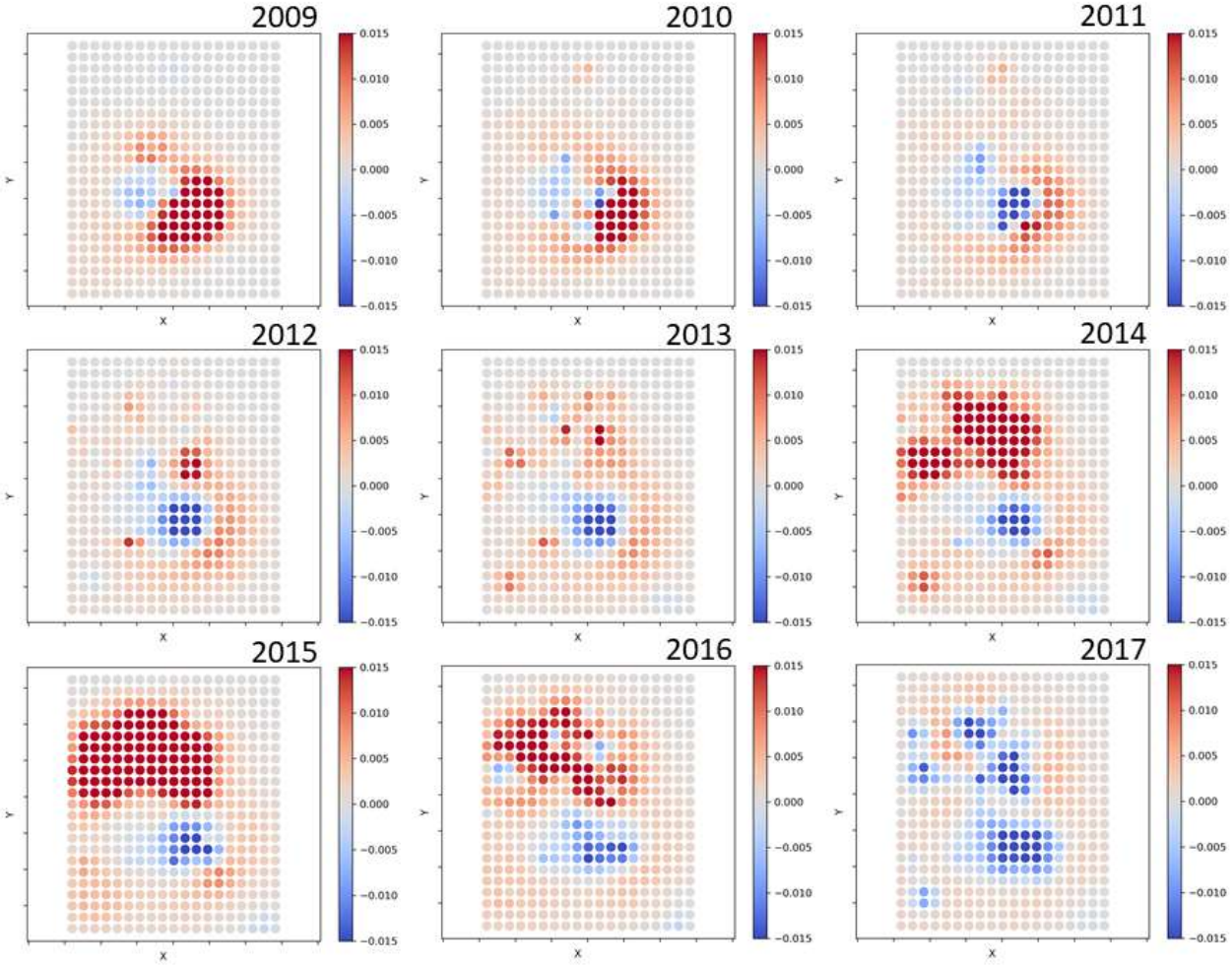

Figure 4: *Coulomb stress rate fields (in MPa/Year) at 4km depth along the basement faults (same X-Y scale as Figure 3).*

2.3 INDUCED SEISMICITY

The traditional Coulomb failure model predicts that whenever the Coulomb stress reaches a threshold value, an earthquake is generated. Assuming a population of faults on which the pre-stresses are uniformly distributed up to the threshold value, the Coulomb failure model depicts direct proportionality between the seismicity rate and the Coulomb stress rate. For example, during any arbitrary stressing history, the Coulomb failure model predicts an instantaneous reduction or rise of seismic events as soon as the Coulomb stress starts to decrease/increase. This prediction is not in agreement with the observed seismicity in central

Oklahoma since only a few observed events have been recorded in the year 2009 (cf. Section 2.4). The Coulomb failure model would predict a high seismicity rate that is linearly related to the high Coulomb stress rate in 2009 (*Figure 4*).

One shortcoming of the Coulomb failure model is that it does not honor the frictional constitutive behavior of faults. Laboratory data show that the timing of dynamic instability of faults depends on initial stress conditions, fault properties and applied stress (Dieterich and Kilgore, 1996). Rate-and-state friction laws have been established in order to reproduce these laboratory observations (see Marone, 1998 for a review). More specifically, the rate-and-state friction laws reproduce the fact that the onset of frictional sliding is a non-instantaneous time-dependent process (as opposed to the instantaneity assumption of the Coulomb model), which introduces a time-dependent failure mechanism for the generation of earthquakes. Now assuming a population of faults following a rate-and-state frictional behavior, and where the time-to-failure of the nucleation spots along the faults is uniformly distributed, Dieterich (1994) derived the following seismicity rate model:

$$R_D = \frac{r_0}{\gamma \dot{S}_0} \quad \text{where} \quad \frac{d\gamma}{dt} = \frac{1}{A\sigma_n'}\left[1 - \gamma \frac{dS}{dt}\right] \tag{2}$$

and where R_D is the seismicity rate, γ is a state variable, S is the modified Coulomb stress function defined in equation (1). The constant r_0 is the steady-state background seismicity rate at the reference stressing rate $\dot{S}_0$. A is a dimensionless fault constitutive parameter.

Segall and Lu (2015) reformulated this seismicity rate equation to eliminate the state variable γ. They defined a normalized seismicity rate, relative to the background rate, as:

$$R = \frac{R_D}{r_0} \tag{3}$$

The differential equation for R, derived from equations (2) and (3), is:

$$\frac{dR}{dt} = \frac{R}{t_a}\left[\frac{\dot{S}}{\dot{S}_0} - R\right] \tag{4}$$

where $t_a = A\sigma_n'/\dot{S}_0$ is the characteristic time delay for the earthquake nucleation process. This delay also corresponds to the time scale of the decay in aftershock rate from the main shock back to the background rate.

2.4 DECLUSTERING OF THE OBSERVED SEISMICITY

The earthquake catalogue used for our study has been compiled by the Oklahoma Geological Survey. The minimum magnitude considered for our analysis is Mw = 3. Only the events nucleating between 3 km and 7 km depth are selected. When this magnitude and depth filtering is applied to the raw earthquake catalogue, the maximum yearly rate of events at Oklahoma reaches roughly 400 events/year in 2015 (*Figure 5*).

One of the assumptions in Dieterich's seismicity rate theory (Dieterich, 1994) that is subject of debate, is the lack of interactions between seismic sources. More specifically, Dieterich's seismicity rate theory assumes aftershocks are directly triggered by the stress changes induced by the mainshock. Effect of stress interactions between aftershocks is not accounted for. To circumvent this potential shortcoming of Dieterich's theory, we apply the declustering algorithm of Zaliapin and co-workers (Zaliapin et al. 2008, Zaliapin and Ben-Zion 2013, Zaliapin and Ben-Zion 2016). This algorithm resolves complete triggering chains based on the relative space-time-magnitude distances, originally introduced by Baiesi and Paczuski (2004). Only the main ingredients of the approach are given below, but the reader is referred to the papers of Zaliapin and co-workers for more details.

The declustering algorithm of Zaliapin et al. (2008) is based on space-time-magnitude distances between earthquakes i and j defined as (Baiesi and Paczuski 2004):

$$\eta_{ij} = \begin{cases} t_{ij}(r_{ij})^d 10^{-bm_i}, & t_{ij} > 0; \\ \infty, & t_{ij} \leq 0. \end{cases} \qquad (5)$$

t_{ij} is the event intercurrence time in years, which is positive if event j occurred after event i ($t_{ij} = t_j - t_i$); $r_{ij} \geq 0$ is the spatial distance between the earthquake hypocenters in kilometers; m_i is the magnitude of event i; d is the (possibly fractal) dimension of the hypocenters; and b corresponds to the b-value of the Gutenberg-Richter frequency-magnitude distribution.

The nearest-neighbor distance for a given event j is the minimum distance among η_{ij} where i goes over all earlier events in the catalogue. The event i that corresponds to the nearest-neighbor distance is called the nearest-neighbor, or parent, of event j.

Zaliapin et al. (2008) proposed to consider the scalar distance η in terms of its space and time components normalized by the magnitude of the parent event i as:

$$T_{ij} = t_{ij}10^{-qbm_i}; \quad \mathcal{R}_{ij} = (r_{ij})^d 10^{-pbm_i}; \quad p + q = 1; \qquad (6)$$

And now:

$$log_{10}\,\eta_{ij} = log_{10}\,T_{ij} + log_{10}\,\mathcal{R}_{ij}. \qquad (7)$$

For our analysis, we fix $b = 1$, $d = 1.6$, and $p = 0.5$ following Zaliapin and Ben-Zion (2016). Zaliapin and Ben-Zion (2013) have demonstrated that the estimated cluster structure is stable with respect to the parameter values. Accordingly, our conclusions are expected to be non-sensitive to the precise parameter values.

Zaliapin et al. (2008) and Zaliapin and Ben-Zion (2016) have shown that observed seismicity generally presents a bimodal joint distribution of ($log_{10}T$, $log_{10}\mathcal{R}$). In the present Oklahoma injection case, one mode corresponds to the independent mainshocks, whereas the other consists of clustered aftershock events located considerably closer in time and space to their parents. *Figure 5* shows the 2D joint distributions of the rescaled time and space component (T, $\mathcal{R}$) of the nearest-neighbor earthquake distance η. For Oklahoma, after applying the declustering step, the maximum yearly rate of mainshocks reaches roughly 120 event/year in 2015 (see *Figure 5*).

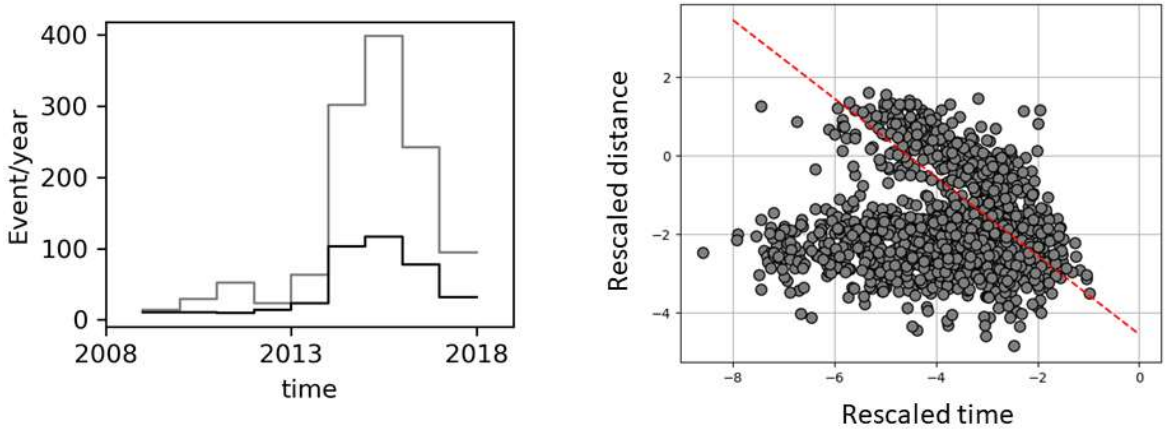

Figure 5: Declustering effect providing a separation between mainshocks and aftershocks induced by injection activities Left: all events of the catalogue (grey line) and independent mainshocks (black line). Right: Bimodal distribution of time and space components ($log_{10}T$, $log_{10}\mathcal{R}$) of the nearest-neighbor distance η. Each gray circle in these plots corresponds to an event in the seismicity catalogue. The location of the event in the ($log_{10}T$, $log_{10}\mathcal{R}$) plane provides information about the time and space distance to the event's parent. The threshold value $log_{10}\eta_0$ to separate the two modes is estimated used a 1D Gaussian mixture model applied to the logarithmic nearest-neighbor distances $log_{10}\eta_{ij}$ (Hicks, 2011). The red dashed diagonal lines depict the $log_{10}\eta_0$. On the right of the red dashed diagonal line, independent mainshocks are indicated, while events on the left of the line are clustered aftershocks.

2.5 DATA ASSIMILATION

The objective of the *data assimilation* procedure is to determine the set(s) of model parameters in Dieterich's (1994) seismicity rate theory (cf. Eq. 4) that give the best agreement between the observed seismicity rate and the computed rate.

In order to compare the computed seismicity rates to the observed ones, both uncertainties in model (e.g., pore pressure distribution, fault orientation, stress calculation) and data (e.g., earthquake location) should be accounted for. We employed a Gaussian smoothing σ_s to the R_D fields to incorporate uncertainties. As a result, the parameter set that needs to be optimized contains four parameters, i.e. $[A, r_0, \dot{S}_0, \sigma_s]$ (see previous section for definition of symbols).

The log-likelihood is defined as the logarithm of the probability that one specific model (with one specific set of model parameters) has generated the observed earthquake catalog. For each set of model parameters the posterior log-likelihood is calculated in order to rank the models (Ogata, 1998; Zhuang et al., 2012). The model with the highest log-likelihood is most likely to have generated the observed seismicity catalogue. For our non-homogeneous stationary Poisson process, and for a given time interval $[t_0, t_1]$ and spatial area $[x_0,x_1]$ x $[y_0,y_1]$, the log-likelihood with respect to N observed earthquakes which have occurred at times t_i and locations (x_i,y_i) is defined by the following function:

$$ll = \sum_{i=1}^{N} \log\left(R_{D\_smo}(xi, yi, ti)\right) - \iiint_{t0,x0,y0}^{t1,x1,y1} R_{D\_smo}(x, y, t)\, dx\, dy\, dt \qquad (8)$$

Following a Bayesian approach, and because we do not have a prior preference for the shape of the distribution of each model parameter, we attribute a bounded uniform a-priori probability distribution for each model parameter. The Markov Chain Monte Carlo (MCMC) algorithm is used to condition the data with these a-priori uniform distributions.

The start of the time period where the data assimilation procedure is deployed is 1st January 2009, start of the observed seismicity, ending on 31 December 2017. Note that we apply our analysis to seismicity rate only. Incorporation of seismic magnitude requires further steps in the approach. Ideally, a joint log-likelihood is applied to assimilate both seismicity rate and seismic magnitude. However, in order to properly model the magnitude of induced events, a much more complex modelling strategy is required combining the nucleation

rate from Dieterich's (1994) theory with, for example, the state of stress and energy available around each nucleation point (e.g., Noda et al., 2009; Schmitt et al., 2015; Dempsey and Suckale, 2016). As performed in previous studies at Oklahoma (e.g. Zhai et al., 2019), the nucleation rate could be combined with an arbitrary spatio-temporally frequency-magnitude distribution that is uniform and constant. However, applying such a procedure would bring additional uncertainties and, for the current purpose of the study, little additional value. Therefore, we focus the analysis on nucleation rate of seismic events alone.

2.6 CONSTRAINED OPTIMIZATION

After applying the data assimilation procedure, the best set of model parameters can be selected with which our predictive model is more likely to explain the observed induced seismicity rate. Using this calibrated predictive model and set of model parameters, the optimum injection strategy is determined. The aim is to prevent the peak of seismicity kicking off in 2014, while at least the same volume of injected brine is injected as has been historically reported for the area. The objective is to maximize the total cumulative field-wide injected brine volume. We include a threshold value for the seismicity rate as a constraint that cannot be exceeded. The objective (maximizing injected volume) and the constraint (minimizing seismicity rate) are expected to be conflicting. The identification of an injection strategy that meets both our objective and constraint is a complex task. The complexity is increased by the non-regular distribution of wells, and the time-dependency of the geomechanical-seismological response (linking pore pressure diffusion and earthquake nucleation) to changes in injection rate. We therefore adopt a numerical optimization approach that aims to solve the following formalized problem:

$$\hat{u} = \underset{u}{\operatorname{argmax}} J(u) \text{ subject to } R(u) < R_{max} \; ; \; J(u) > J_{min} \qquad (9)$$

The control vector u contains the well injection rates which are constant during discretized time intervals, i.e. $u = [u_1^1, u_2^1, \dots, u_{N_t}^1, u_1^2, \dots, u_{N_t}^{N_w}]$ where the subscripts indicate the time interval, and the superscripts indicate the well. The total number of controls is expected to be very large in our scenario since there are more than 200 wells and multiple time intervals. $J(u)$ is the total volume of injected brine, and $R(u)$ is the maximum field-wide yearly event rate. J_{min} and R_{max} are the historical total cumulative field-wide injected brine volume from January 1995 to January 2018, and the threshold value of the field-wide yearly event rate during the same time period, respectively.

We use the Stochastic Simplex Approximate Gradient (StoSAG) estimation method where the gradients are used in an advanced method for constrained optimization (Chen et al., 2009; Fonseca et al., 2014; 2017). An ensemble of randomly chosen control vectors (well injection rates) is generated and the stochastic gradient, total volume of brine injected and yearly event rate are computed. Based on the stochastic gradient direction, the controls are updated, and a new ensemble of perturbed controls is regenerated. This iterative process continues until there are no more significant changes in the total amount of brine injected or controls, or when a maximum number of iterations is reached (*Figure 6*). As an initial estimate for the controls we prescribe constant and equal rates for all wells, so that the cumulative injected volume matches the historical total injected volume.

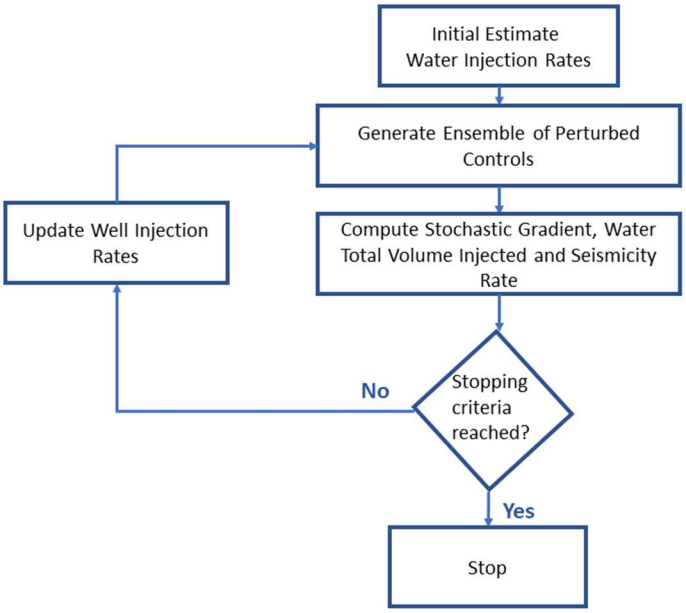

Figure 6: *Constrained optimization scheme.*

3 Results

3.1 POSTERIOR MODEL PARAMETERS OF THE UNSTEADY OKLAHOMA FAULT SYSTEM

The joint and marginal posterior probability distributions of the model parameters obtained after assimilation of the declustered catalogue over the period from 1st January 2009 to 31 December 2017 are well constrained (*Figure 7*). The median of the marginal posterior distributions of each model parameter define the best posterior estimates ($A = 0.00027, r_0 = 18\ event/year, \dot{S}_0 = 0.0004$ MPa/year, $\sigma_s = 34\ km$). With our modelling approach, the average effective normal stress is 44 MPa at 4km depth, which leads to the best posterior estimate of the characteristic relaxation time of seismicity, $t_a = \frac{A\sigma_n'}{\dot{S}_0} = 29.7\ years$.

The assimilation of observed events starts in 2009 when a significant earthquake activity started to be recorded. Consequently, the Dieterich (1994) seismicity rate equation (4) is solved assuming initial condition at steady state, that is $R(0) = 1$ in 2009. However, the start of the human-induced perturbation of the Oklahoma system by massive brine injections goes back to 1995, and hence it is most likely that the background activity was not at steady state in 2009. In fact, defining $R' = \beta R$ and by operating a change of variable, we can show that R' satisfies an equation similar to equation (4) and reads:

$$\frac{dR'}{dt} = \frac{R'}{A\sigma_n'/\dot{S}_0'}\left[\frac{\dot{S}}{\dot{S}_0'} - R'\right] \qquad (10)$$

with the unsteady initial condition $R'(0) = \beta$ in 2009, and the background stressing rate $\dot{S}_0' = \dot{S}_0/\beta$. Following equation (3), this solution corresponds to a background seismicity rate $r_0' = r_0/\beta$. This mathematical derivation implies that the background stressing rate $\dot{S}_0'$ and background seismicity rate r_0' were $1/\beta$ times lower in 1995, at the start of injection when the Oklahoma system is assumed to be steady, compared to the values of $\dot{S}_0$ and r_0 inferred for 2009. The fault constitutive parameter A is expected to remain constant in time. However, the background stressing rate and seismicity rate inferred for 2009 should not be interpreted as real steady state background values (before the start of human-induced perturbations by brine injections), but should be understood as “apparent background values”, which are actually the reference values at the initial time of the analysis, here 2009. The fact that the Oklahoma fault system was probably never at steady state since the

start of injection is an important aspect to acknowledge. During this transient phase caused by massive saltwater injections, the *apparent* background stressing rate and background seismicity rate are constantly increasing up to reaching the next steady state.

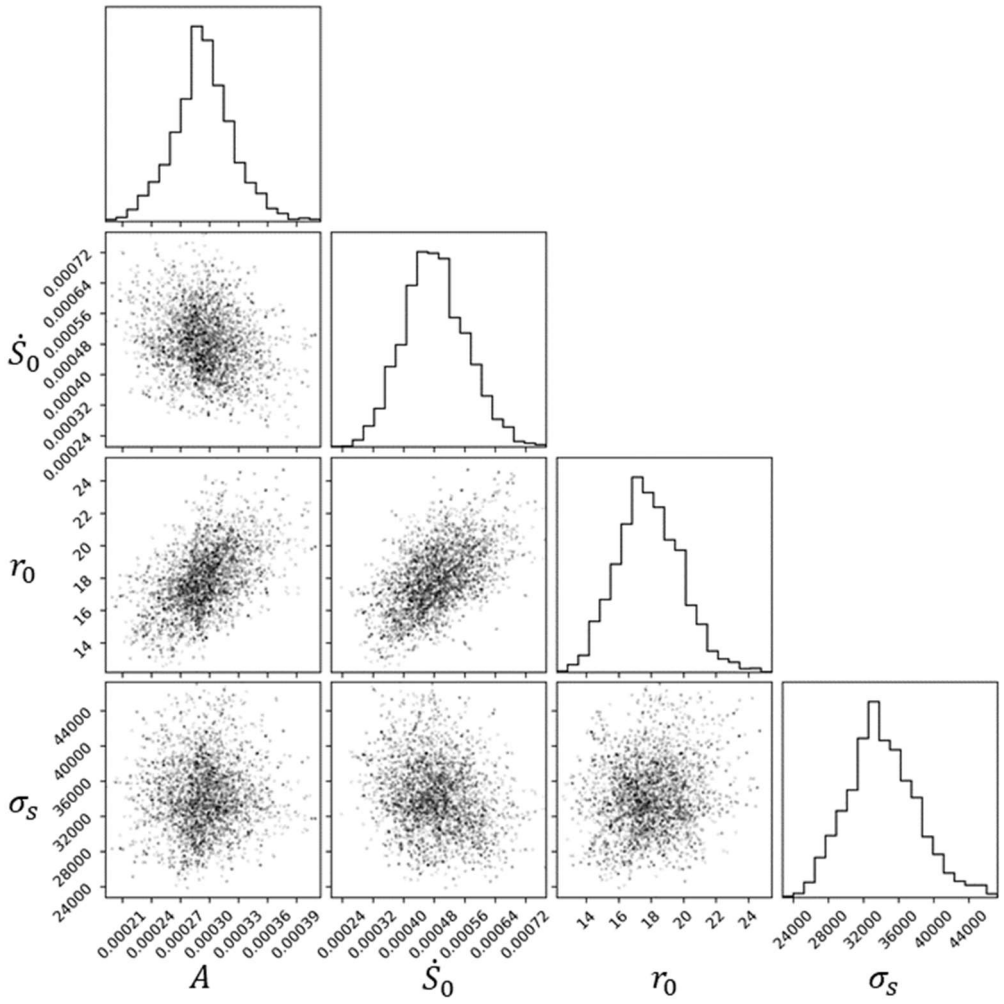

Figure 7: *Marginal and joint probability distributions of model parameters obtained with the MCMC search. Bounded uniform prior distributions for each model parameters are: A: U($1e^{-5}$, 1.0), $\dot{S}_0$: U($1e^{-7}$, 1.0), r_0: U(0.001, $2e^5$), σ_s: U(1000, 50000) - with U(a, b) is a uniform distribution between a and b.*

3.2 TEMPORAL PATTERN

A posterior ensemble of temporal yearly event rate predictions can be visualized by randomly picking members from the posterior density distributions obtained with the MCMC search. This ensemble can be compared with the data. However, it should be noted that the modelling strategy does not yet include the intrinsic Poisson variability of earthquake occurrence. The observed declustered catalogue is considered here as one unique realization of a stochastic, non-stationary Poisson process. Each posterior member of the modelling approach is one particular model of the time-dependent seismicity rate underlying the Poisson process. For an appropriate assessment of the predictive performance of our models, the stochastic Poisson variabilities need to be accounted for. For each posterior member, which can be considered as the mean of an underlying Poisson distribution, multiple synthetic catalogues are generated where the likelihoods of the event location and timing are proportional to the event density (Zhuang and Touati, 2015). *Figure 8* shows that the posterior

predictions capture very well the temporal variation in observed seismicity. More specifically, our modelling strategy can predict:

(1) the relative seismicity quiescence from 2009 to 2013,
(2) the abrupt ramp-up of the seismicity rate starting in 2014,
(3) the fast decrease of the seismicity rate starting in 2016 by the new measures imposed by the regulators.

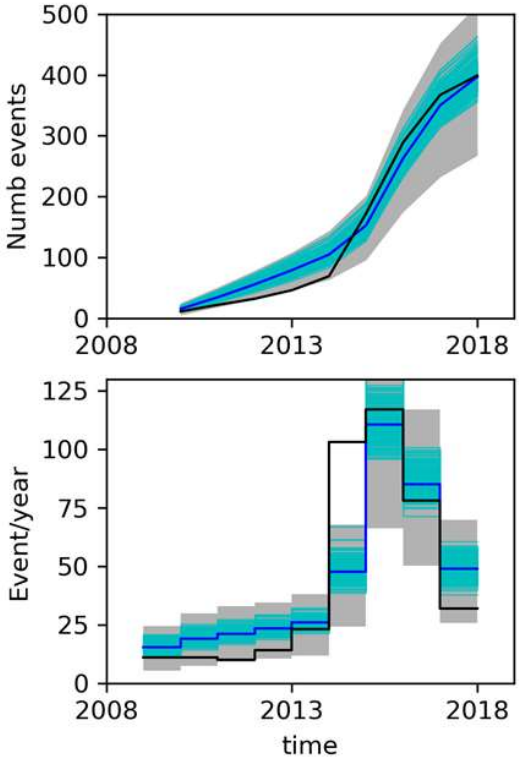

Figure 8: Comparison of the predicted seismicity histories with the data (black line). The model corresponds to 300 realizations (cyan) randomly drawn from the posterior density distribution obtained with the MCMC search during calibration. The mean of the models is indicated by the blue line. For each posterior member, 30 synthetic catalogues are generated in order to account for stochastic Poisson variabilities. The grey region indicates 95% of the distribution of the 9000 synthetic catalogues when stochastic Poisson variabilities are accounted for. Top: cumulated number of events. Bottom: yearly event rate.

3.3 SPATIAL PATTERN

Predictions of spatial distribution of seismicity rate based on our modelling strategy can also be evaluated. *Figure 9*, *Figure 10* and *Figure 11* show a comparison of the spatio-temporal distribution observations and model forecasts for the relative seismicity rate, the smoothed event density, and the smoothed cumulative even density, respectively. For each of these figures, the median of the ensemble of posterior realizations is displayed. The overall spatio-temporal evolution of the observed seismicity is well reproduced by our modelling strategy. More specifically, the observed and modelled seismicity both start to increase (in 2009) at the center of the area of interest (i.e. central Oklahoma) and then progressively migrate outwards to finally be concentrated in the North-West.

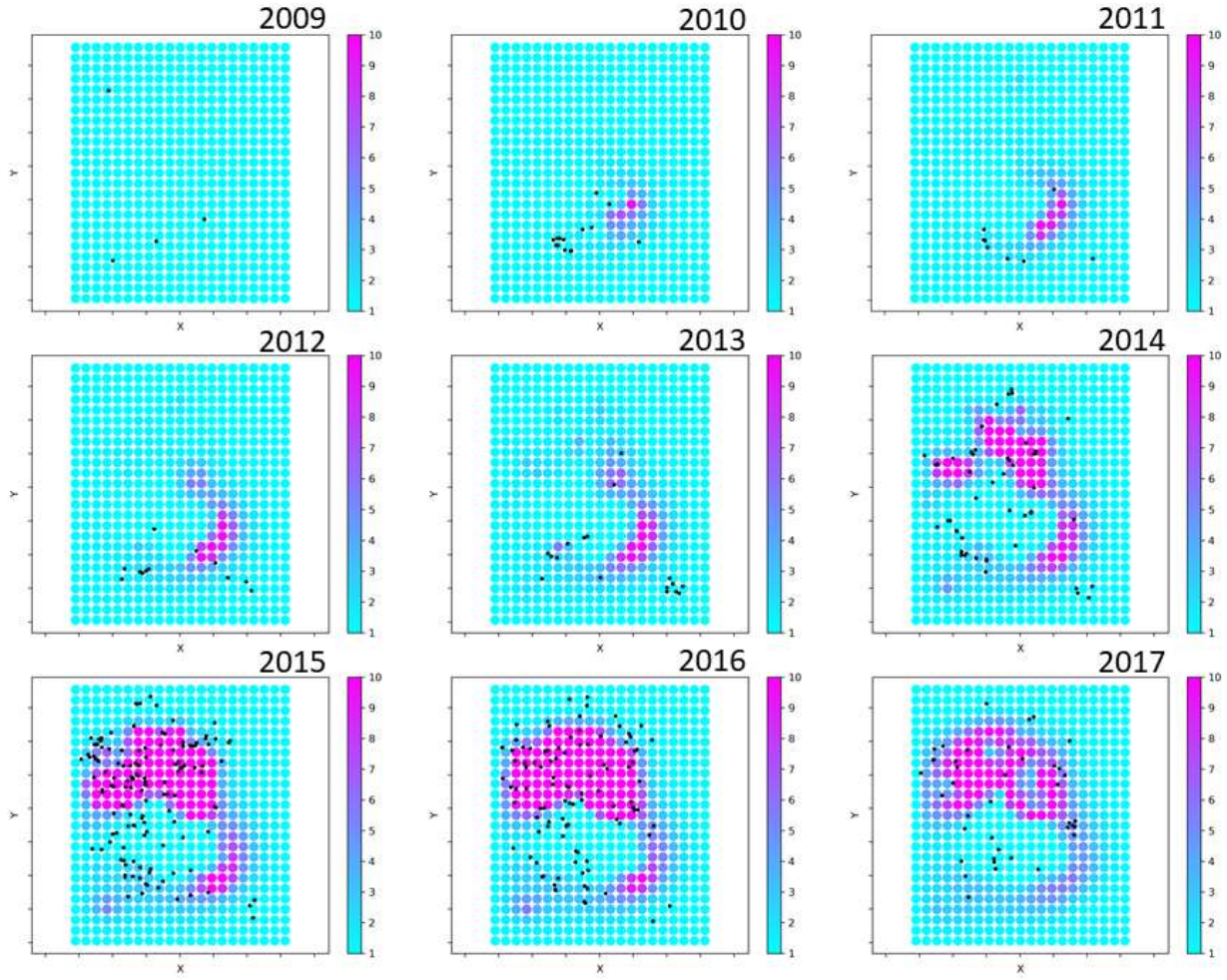

Figure 9: Mean posterior fields of relative seismicity rate (/year) at 4km depth along the basement faults (same X-Y scale as Figure 3). The black dots indicate the observed events.

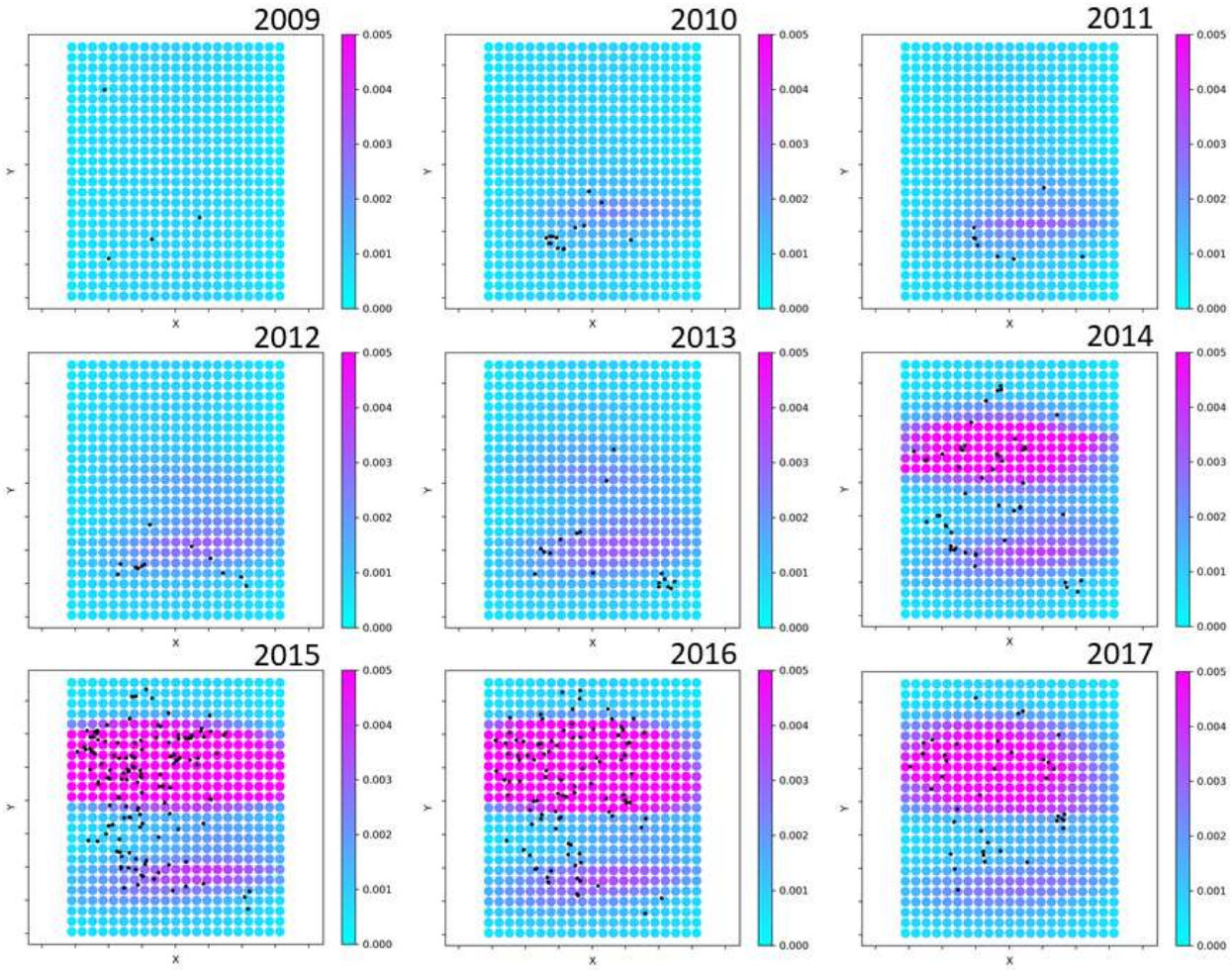

Figure 10: Mean posterior fields of smoothed event density (/km^2) at 4km depth along the basement faults (same X-Y scale as Figure 3). The black dots indicate the observed events.

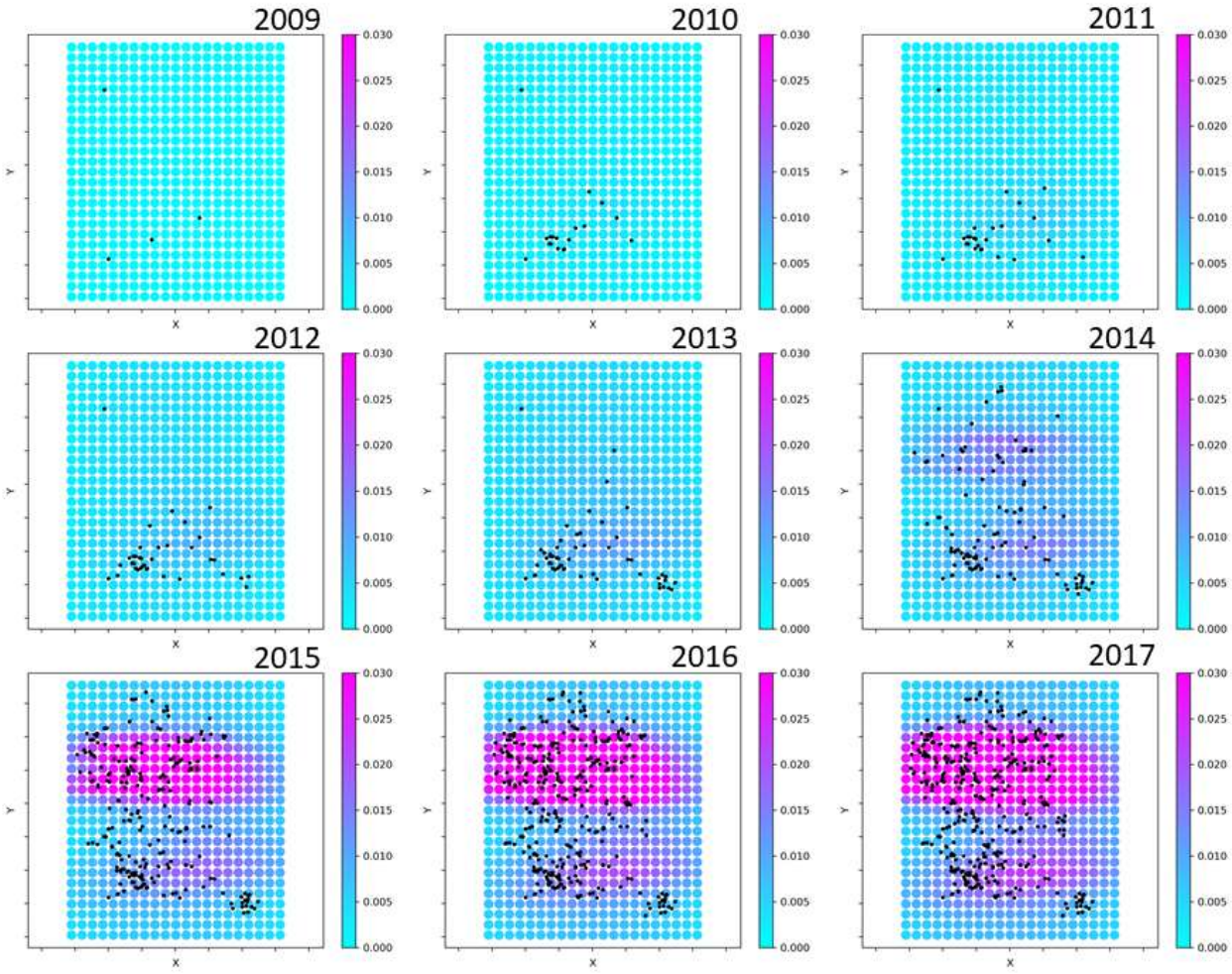

Figure 11: Mean posterior fields of smoothed cumulated event density (/km^2) at 4km depth along the basement faults (same X-Y scale as Figure 3). The black dots indicate the observed events.

3.4 TOWARDS AN OPTIMUM INJECTION STRATEGY

Two optimization experiments have been performed. For both experiments we seek to find the optimum injection strategy for each well leading to a total volume of injected brine that is at minimum equal to the total historic injected volume while keeping the yearly event rate below a certain threshold. This threshold is set to 25 events/year in order to avoid the peak of seismicity rate starting in 2014.

For the first experiment, we define one constant injection rate for each well during the entire history of injection (from January 1995 to January 2018) and estimate the seismicity rate based on one unique simulated pressure field output at the end of 2017. For a more elaborate estimate of the seismicity rate, the pressure fields should be simulated on a yearly basis. However, the focus of this experiment is to test the performance of the optimizer. For each iteration, the number of perturbations is set to 50 to appropriately compute the stochastic gradients. The optimizer successfully converged towards an optimum solution which satisfies both constraints: (1) the total volume injected is more than twice the historical total volume injected, and (2) the yearly event rate is 20.02 which is below the threshold of 25 event/year.

After gaining confidence in the performance of the optimizer with the first experiment, a more complex and realistic experiment is performed with well controls that can be adjusted every 5 years and with pressure fields and simulated seismicity rates that are provided yearly. For this second experiment, 100 perturbations are used to compute the stochastic gradient. The optimized strategy leads to 1.7 times more brine stored relatively to the historical total injected volume (*Figure 12*), and the maximum yearly event rate remains at 22.5, below the imposed threshold of 25 event/year. To reach this optimum injection strategy, the field-wide yearly injection

rate needs to be kept almost constant during the entire injection period. This strategy results in a roughly linear increase of the cumulative total volume with time (Figure 12).

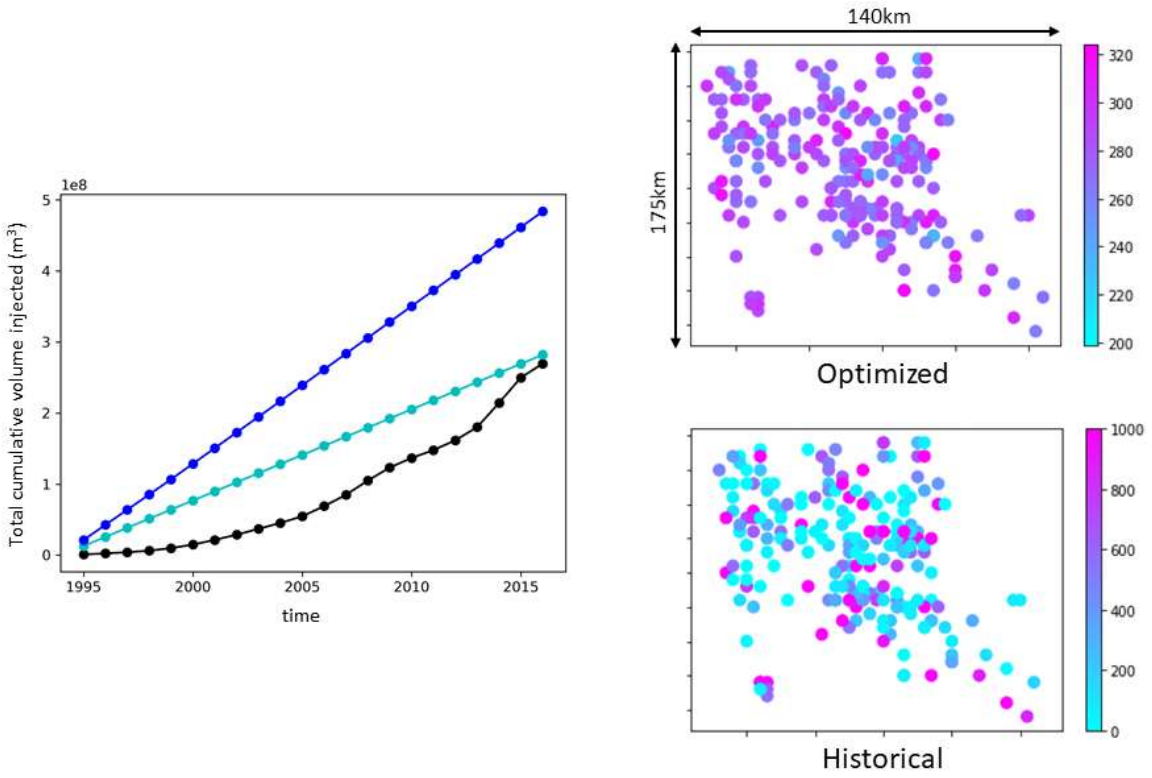

Figure 12: Optimized injection strategy. Left: field-wide cumulative volume of injected saltwater (historical scenario in black, initial estimate for the optimization experiment in cyan, and optimum scenario in blue). Right: well injection rates (m^3/day) in 2015 for the historical (bottom, the color scale is defined with a maximum of 1000 m^3/day) and optimized scenario (top).

At the optimum strategy, the spatial distribution of the injection rates at each well, even if heterogenous, presents a lower variability relatively to the historical scenario (*Figure 12*). Distributing more uniformly in space and time the injected volume of brines, the optimum strategy leads to more uniform spatio-temporal pore pressure changes (*Figure 13*). Consequently, the Coulomb stress rates (induced by both the direct pore pressure changes and the poro-elastic loading) are more uniformly distributed and remains relatively lower as shown for 2015 in *Figure 13*. More specifically, the localized high Coulomb stress rates at the origin of the historical peak in seismicity starting in 2014 are prevented.

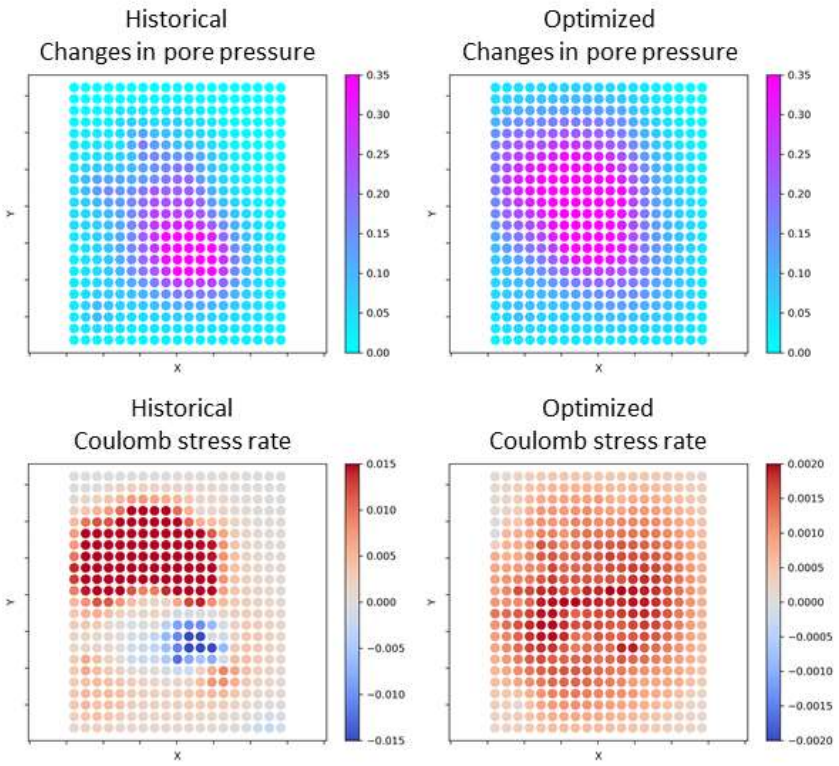

Figure 13: Comparison of the changes in pore pressure (up, in MPa) and Coulomb stress rate (down, in MPa/year) in 2015 between the historical (left) and optimized (right) scenarios. All the fields are assessed at 4km depth along the basement faults, and the same X-Y scale as Figure 3 is used. Note the difference in the color scale between the historical and optimized Coulomb stress rate.

4 Concluding Discussion

We present a three-step constrained optimization workflow that outlines injection scenarios for maximizing injected volume under a constraint imposed by seismicity rates. It represents a physics-based predictive workflow that ensures that simulated seismicity is consistent with observed seismicity. For massive wastewater injection around Oklahoma, the workflow can test multiple injection scenarios to find an optimum scenario which maximizes the total volume injected while avoiding the sharp increase of seismicity as observed in 2014. This increase led to the regulatory measures and ultimately to the shut-down of the injection.

In the first step of the workflow, a forward modelling strategy is designed that honors as much as possible all available prior knowledge from central Oklahoma. It includes information on (i) geology and flow which are used to set up flow simulations, and (ii) in-situ stress conditions, fault orientations, observed seismicity and prime physical processes controlling it, which are used to deploy the geomechanical and seismological analysis. Flow simulations are performed by using the open source OPM-FLOW simulator which uses historical monthly injection rates of each well at central Oklahoma as input. With the approach, robust spatio-temporal pressure distributions have been computed, including complex flow interaction between the more than 200 wells at central Oklahoma. With the simulations, the pore pressure at the nucleation depth of seismic events (placed at 4 km depth based on observations) in the basement was accurately captured. These changes in pore pressure are the main drivers of the two physical processes controlling the nucleation of induced earthquakes in central Oklahoma: the direct decrease in the effective normal stress at fault due to the pore pressure increase (Norbeck and Horne, 2016; Langenbruch and Zoback, 2016; Dempsey and Riffault, 2019), and the poro-elastic loading caused by the changes in the rock volume when its pore pressure is increased (Goebel et al., 2017; Zhai et al., 2019). The stress contribution from the poro-elastic loading has been derived from the mechanical simulator MACRIS (van Wees et al., 2019; Candela et al., 2019). MACRIS is based on a newly developed mesh-free approach, which can (1) directly use 3D pressure fields from OPM-FLOW as input for geomechanical modelling, and (2) acquire high stress resolution at the interface of interest (the horizontal-

plane at 4km depth in the Oklahoma case). Coulomb stress changes have been combined with Dieterich's theory (Dieterich, 1994) to model the spatio-temporal evolution of the seismicity rate.

In the second, step the seismicity data is assimilated in order to update the model parameters of the forward model from the first step. Data assimilation is used to assess the predictive power of the forward model by comparing simulated and historical seismicity rates. This assimilation step has often not been considered in previous studies of induced seismicity at Oklahoma injection sites. Generally, a sensitivity analysis for temporal predictions of induced seismicity is performed (e.g., Zhai et al., 2019). In the current workflow, the seismicity data has been assimilated in both space and time (see also Candela et al., 2019). It has been demonstrated that the distribution of seismicity in both space and time can be used to constrain the posterior distributions of model parameters. We showed that the field-wide modelled yearly event rate and the modelled spatio-temporal event density are both successfully capturing the spatio-temporal distributions of observed events. It confirmed the predictive power of our modelling strategy that aims to honor the ensemble of available prior information for the Oklahoma injection sites. Although not performed in the present study, the results suggest that the approach is suitable to forecast the potential return of the Oklahoma induced seismicity to the background rate following the arrest of all injection activities (Langenbruch et al., 2018; Zhai et al., 2019).

In the third step, an optimization approach is outlined that aims to find an optimum spatio-temporal injection scheme in order to maximize the total volume injected while keeping the seismicity rate below a cap. The cap is chosen so that the stop of the injection activities in April 2017 may be prevented as seismicity remains below a threshold value.

The present study combines both cutting-edge physics-based predictive models with a cutting-edge optimization algorithm. Despite that the modelling framework is applied to the Oklahoma case study, the primary objective was to demonstrate that complex optimization problems with two conflicting objectives involving full physics-based models for flow, geomechanics and induced seismicity can be solved. The modelling framework is based on existing workflows that were originally deployed for the optimization of well planning for hydrocarbon recovery (Chen et al., 2009; Fonseca et al., 2014; 2017), and adjusted for the specific constrained optimization problem. As such this modelling framework can thus be seen as generic and can be applied to other instances of anthropogenic subsurface activities as for example but not limited to that carbon storage and sequestration.

We showed that it likely would have been possible to avoid the dramatic rise of the rate of seismicity starting in 2014 while still injecting a total volume of fluid that is ~1.7 times larger than the historical injected volume. The optimum strategy involved more uniform spatio-temporal distributions of the injection rates, resulting in changes in pore pressure that are smoother and more uniformly spread in space and time relatively to the historical scenario. The use of injections at peripheral wells (that is distributed at the edges of the area of interest) were favored in order to prevent clustering of well injection activities in space and time that caused the historical high seismicity rates.

More constraints should be added to the present approach in order to include additional key factors which have influenced the spatio-temporal historical distribution of the injection rates. As an example, the use of wells for injection should be constrained by additional parameters such as the supply of hydraulic fracturing and formation fluids from nearby shale gas sites as the fluid brine injected in the Arbuckle aquifer is a waste-product of production of shale gas. Accordingly, a spatio-temporal correlation between injection volumes and shale gas operations in the area is likely. In the current optimization example, it is assumed that all wells were available at any moment in time. One way to honor the correlation between shale gas operations and injection is to add a cost constraint in the optimization, i.e. injections via wells that were not used in historical injection should be penalized with a higher cost. This additional implementation can be achieved with the present optimization algorithm.

5 References

Alt RC & Zoback MD. 2016. In situ stress and active faulting in Oklahoma. Bulletin of the Seismological Society of America 107(1):216-228.

Baiesi, M., and M. Paczuski. 2004. Scale-free networks of earthquakes and aftershocks, Phys. Rev. E, 69, 066106.

Barnes, J. and Hut, P. 1986. A hierarchical O(N log N) force-calculation algorithm. Nature, 324, 446-449.

Chen Y, Oliver DS, Zhang D. 2009. Efficient ensemble-based closed-loop production optimization. SPE Journal, 14(4):634–645.

Candela, T., Osinga, S., Ampuero, J.P., Wassing, B., Pluymaekers, M., Fokker, P.A., van Wees J.D., de Waal, H.A., Muntandam-Bos, A.G. 2019. Depletion-induced seismicity at the Groningen gas field: Coulomb rate-and-state models including differential compaction effect, Journal of Geophysical Research: Solid Earth 124, 7081.

Dempsey, D., Riffault, J. 2019. Response of induced seismicity to injection rate reduction: Models of delay, decay, quiescence, recovery, and Oklahoma. Water Resources Research, 55, 656–681. https://doi.org/10.1029/2018WR023587.

Dieterich, J.H. 1994. A constitutive law for rate of earthquake production and its application to earthquake clustering, Journal of Geophysical Research, 99, 2601.

Dieterich, J. H., and B. Kilgore. 1996. Implications of fault constitutive properties for earthquake prediction, Proc. Natl. Acad. Sci., 93(9),3787–3794.

Ellsworth, W.L. 2013. Injection-induced earthquakes. Science 341, 1225942. https://doi.org/10.1126/ sciadv.1500195.

Faith JR, C.D. Blome, M.P. Pantea, J.O. Puckette, T. Halihan, N. Osborn, S. Christenson, S. Pack. 2010. Three-dimensional geologic model of the Arbuckle-Simpson Aquifer, south-central Oklahoma. (US Geological Survey).

Fonseca, R.M.M., B Chen, JD Jansen, A Reynolds. 2017. A stochastic simplex approximate gradient (StoSAG) for optimization under uncertainty. International Journal for Numerical Methods in Engineering 109 (13), 1756-1776.

Fonseca, R.M.M., AS Stordal, O Leeuwenburgh, PMJ Van den Hof, JD Jansen. 2014. Robust ensemble-based multi-objective optimization. ECMOR XIV-14th European conference on the mathematics of oil recovery.

Geertsma, J. 1973. A Basic Theory of Subsidence Due to Reservoir Compaction: the homogeneous case, Verh. Kon. Ned. Geol. Mijnbouwkundig Genootschap, 28, pp 43-62.

Goebel, T. H. W., Weingarten, M., Chen, X., Haffner, J. & Brodsky, E. E. 2017. The 2016 Mw5.1 Fairview, Oklahoma earthquakes: Evidence for long-range poro-elastic triggering at >40 km from fluid disposal wells. Earth Planet. Sci. Lett. 472, 50–61, https://doi. org/10.1016/j.epsl.2017.05.011.

Goebel, T.H.W., Walter, J., Murray, K., and Brodsky, E.E. 2017. Comment on: How will induced seismicity in Oklahoma respond to decreased saltwater injection rate. Science Advances doi: 10.1126/sciadv.1700441.

Hicks, A. 2011. Clustering in multidimensional spaces with applications to statistical analysis of earthquake clustering, MSc Thesis, Department of Mathematics and Statistics, University of Nevada, Reno.

Hincks, T., Aspinall, W., Cooke, R. & Gernon, T. 2018. Oklahoma's induced seismicity strongly linked to wastewater injection depth. Science 359, 1251–1255, https://doi.org/10.1126/science.aap7911.

Holland A.A. 2013. Optimal Fault Orientations within Oklahoma. Seismological Research Letters 84(5):876-890.

Johann, L., Shapiro, S.A. & Dinske, C. The surge of earthquakes in Central Oklahoma has features of reservoir-induced seismicity. Sci Rep **8,** 11505 (2018). https://doi.org/10.1038/s41598-018-29883-9.

Johnson KS. 2008. Geologic history of Oklahoma. Earth sciences and mineral resources of Oklahoma: Oklahoma Geological Survey Educational Publication 9:3-5. 346.

Keranen, K.M., M. Weingarten, G. A. Abers, B. A. Bekins, S. Ge. 2014. Sharp increase in central Oklahoma seismicity since 2008 induced by massive wastewater injection. Science 345, 448–451.

Keranen KM, Savage HM, Abers GA, & Cochran ES. 2013. Potentially induced earthquakes in Oklahoma, USA: Links between wastewater injection and the 2011 Mw 5.7 earthquake sequence. Geology 41(6):699-702.

Langenbruch, C., M. D. Zoback. 2016. How will induced seismicity in Oklahoma respond to decreased saltwater injection rates? Sci. Adv. 2, e1601542.

Langenbruch, C., M. Weingarten, M. D. Zoback. 2018. Physics-based forecasting of manmade earthquake hazards in Oklahoma and Kansas. Nat. Commun. 9, 3946.

Marone, C. 1998. Laboratory-derived friction laws and their application to seismic faulting, Ann. Rev. Earth Planet. Sci., 26, 643–696.

McGarr, A., A. J. Barbour. 2017. Wastewater disposal and the earthquake sequences during 2016 near Fairview, Pawnee, and Cushing, Oklahoma. Geophys. Res. Lett. 44, 9330– 9336.

Mindlin, R.D. 1936. Force at a Point in the Interior of a Semi Infinite Solid, Physics, 7, 195-202.

Noda,H., E.M. Dunham, and J.R. Rice. 2009. Earthquake ruptures with thermal weakening and the operation of major faults at low overall stress levels. J. Geophys. Res., 114, B07302, doi:10.1029/2008JB006143.

Norbeck, J. H. & Horne, R. N. 2016. Evidence for a transient hydromechanical and frictional faulting response during the 2011 Mw 5.6 Prague, Oklahoma earthquake sequence. Journal of Geophysical Research: Solid Earth 121, 8688–8705, https://doi.org/10.1002/2016JB013148.

Ogata, Y. 1998. Space-Time Point-Process Models for Earthquake Occurrences. Annals of the Institute of Statistical Mathematics, Volume 50, Issue 2, pp 379–402.

Okada, Y. 1992. Internal deformation due to shear and tensile faults in a half-space, Bull. seism. Soc. Am., 82(2), 1018–1040.

Pei, S., Z. Peng, X. Chen. 2018. Locations of injection-induced earthquakes in Oklahoma controlled by crustal structures. J. Geophys. Res. Solid Earth 123, 2332–2344.

Schmitt, S. V., P. Segall, and E. M. Dunham. 2015. Nucleation and dynamic rupture on weakly stressed faults sustained bythermal pressurization, J. Geophys. Res. 120, no. 11, 7606–7640, doi: 10.1002/2015JB012322.

Segall, P., and S. Lu. 2015. Injection-induced seismicity: Poro-elastic and earthquake nucleation effects, J. Geophys. Res. Solid Earth, 120, 5082–5103, doi:10.1002/2015JB012060.

van Wees J.D., S. Osinga, K. Van Thienen-Visser, and P.A. Fokker. 2018. Reservoir creep and induced seismicity: inferences from geomechanical modeling of gas depletion in the Groningen field, Geophysical Journal International, 212, 1487-1497.

van Wees, J.D., Pluymaekers, M., Osinga, S., Fokker, P.A., Van Thienen-Visser, K., Orlic, B., Wassing, B.B.T., Hegen, D., Candela, T. 2019. 3-D mechanical analysis of complex reservoirs: a novel mesh-free approach, Geophysical Journal International, 219, 1118.

Walsh, F. R. & Zoback, M. D. 2015. Oklahoma's recent earthquakes and saltwater disposal. Sci. Adv. 1,

Weingarten, M., S. Ge, J. W. Godt, B. A. Bekins, J. L. Rubinstein. 2015. High-rate injection is associated with the increase in U.S. mid-continent seismicity. Science 348, 1336–1340.

Zaliapin, I., A. Gabrielov, V. Keilis-Borok, and H. Wong. 2008. Clustering analysis of seismicity and aftershock identification. Phys. Rev. Lett., 101, 018501. doi: 10.1103/PhysRevLett.101.018501.

Zaliapin, I. and Y. Ben-Zion. 2013. Earthquake clusters in southern California, I: Identification and stability. J. Geophys. Res., 118, doi: 10.1002/jgrb.50179.

Zaliapin, I. and Y. Ben-Zion. 2016. Discriminating characteristics of tectonic and human-induced seismicity. Bull. Seismol. Soc. Am., 106(3), 846-859, doi: 10.1785/0120150211.

Zhai, G., M Shirzaei, M Manga, X Chen. 2019. Pore-pressure diffusion, enhanced by poro-elastic stresses, controls induced seismicity in Oklahoma. Proceedings of the National Academy of Sciences 116 (33), 16228-16233

Zhuang, J., D. Harte, S. Werner, M.J., Hainzl, S., and S., Zhou. 2012. Basic models of seismicity: temporal models, Community Online Resource for Statistical Seismicity Analysis, doi:10.5078/corssa-79905851.

Zhuang, J., and S. Touati. 2015. Stochastic simulation of earthquake catalogs, Community Online Resource for Statistical Seismicity Analysis, doi:10.5078/corssa-43806322. Available at http://www.corssa.org.